Tunable infrared detector with integrated micromachined Fabry-Perot filter

Norbert Neumann[a], Martin Ebermann[a], Karla Hiller [b], Steffen Kurth [c]
[a] InfraTec GmbH, Dresden, Germany
[b] Chemnitz Univ. of Technology, Center for Microtechnologies, Chemnitz, Germany
[c] Fraunhofer Institute for Reliability and Microintegration, Chemnitz, Germany

ABSTRACT

This paper reports design, fabrication and test results of a tunable pyroelectric detector with an integrated micromachined Fabry-Perot (FP) filter for gas analysis in the Mid-Wave Infrared (MWIR). The new approach is based on a bulk micromachined Fabry-Perot interferometer with an air cavity, which is electrostatically tuned. Various types of moveable reflectors and spring configurations have been fabricated to determine the optimum solution with respect to maximum tuning range, low gravity influence on center wavelength and suitable filter bandwidth. Short and long cavity filters were designed for the spectral ranges of 3…4.3 µm and 3.7…5.0 µm respectively. The tunable filter is arranged on top of a current mode pyroelectric detector with a flat spectral response. It could be shown that the main challenge is to achieve a high finesse in spite of non-perfect parallelism, mirror curvature and the additional phase shift caused by the Bragg reflectors.

Keywords: Fabry-Perot filter, finesse, Infrared filter, Bragg reflector, anti-reflection coating, bulk micromachining,

1. INTRODUCTION

Infrared pyroelectric detectors equipped with narrow band infrared filters are widely used in infrared analyzers and flame & fire detection systems /1/. Pyroelectric detectors are characterized by room temperature operation, robustness, flat spectral response and low costs. The center wavelength and bandwidth of the commonly used narrow band infrared filters are selected in accordance to the substances to be analyzed. Center wavelength and bandwidth are fixed by the thin film design. The more substances that have to be analyzed simultaneously, the more detectors, or detectors with separate spectral channels, are necessary. Flexibility and performance of a device equipped with a tunable filter are more sophisticated than a simple fixed filter approach because new measuring algorithms are possible particularly if mixtures have to be analyzed in which the substances are characterized by adjacent or overlapping absorption bands.

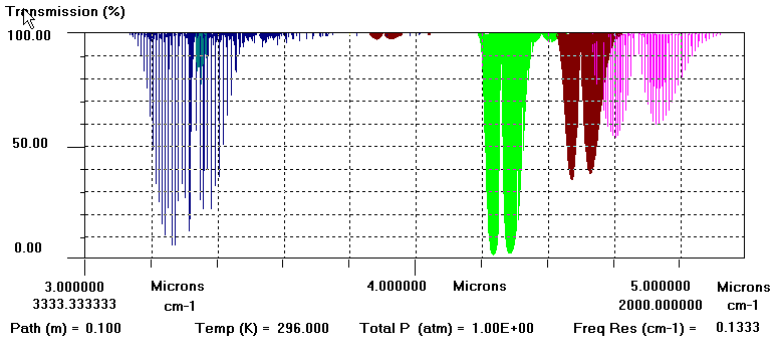

Fig. 1. Transmission of CH_4, C_2H_6, CO_2, CO and N_2O in the 3…5 µm band /2/

The device could be operated like a spectrometer to obtain a spectral signature /3/. The spectral ranges from 8...12 µm and 3...5 µm are often used for the absorption spectroscopy. In the range between 5...8 µm strong absorption bands from water vapor interfere with other bands. In figure 1 the absorption bands of some gases are shown in the range from

3...5 µm as an example. Combustible, toxic or environmental harmful gases like CH_4, C_2H_6, CO, N_2O can be measured in the spectral range of 3…5 µm. This spectral range is also easier to measure, because up to 4.5 µm low cost miniature incandescent lamps can be used as IR source.

Therefore our first aim was, to develop a MEMS based tunable filter for gas analysis in the spectral range of 3…5 µm and to integrate it into a pyroelectric detector. The aperture of the MEMS filter must be several square millimeters and reach a spectral bandwidth of 100 nm. The filter should be able to manage a tuning range of about 2000 nm and should show only a small dependency of the optical filter properties on position and temperature. The peak transmittance should be 70 % and the out-of-band blocking should be better than 0.5 %.

2. FABRY-PEROT FILTER DESIGN

2.1 Optical considerations

A classical Fabry-Perot interferometer is the key element of the MEMS based tunable IR filter, which is built up of an optical resonator consisting of two coplanar reflectors with a separation distance d and a material with a refraction index n in between them. By varying the separation distance d the filter can be spectrally tuned. In figure 2 the set-up principle and the transmission as function of the wavelength λ is presented.

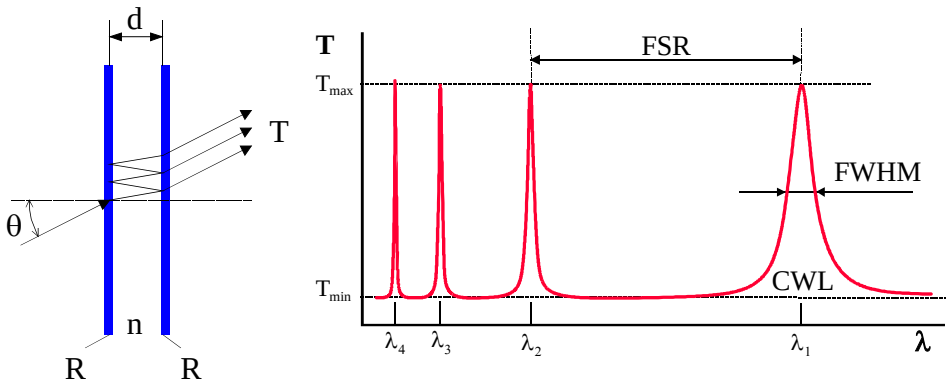

Fig. 2. Schematic arrangement principle and transmission spectra of the Fabry-Perot interferometer

If we take into account the absorptance A and the reflectance R of the reflectors, the transmission T can be described with the Airy-Function /4/:

$$T = \left(1 - \frac{A}{(1-R)}\right)^2 \frac{1}{1 + F\sin^2 \delta/2} \tag{1}$$

with

$$F = \frac{4R}{(1-R)^2} \tag{2}$$

and

$$\delta = 4\pi n d \sigma \cos\theta - 2\varphi(\sigma) \tag{3}$$

where d and n are the physical thickness and refractive index of the resonant cavity, θ the angle of incidence, and φ the phase shift on reflection. F is termed as F-value and δ as optical phase.

The Fabry-Perot interferometer only transmits radiation, which satisfies the interference condition $\delta = m\pi$. The form of individual peaks is $\sin^2(1/\lambda)$ with the maximum transmittance at the center wavelength (*CWL*) λ_m. The period of the Airy function is described as free spectral range (*FSR*) and is constant in respect of the wavenumber, $\sigma = 1/\lambda$ but

continuously decreasing as function of the wavelength λ. The bandwidth of the interference peak at the half-power transmittance $T_{max}/2$ is termed as full-width at half-maximum *(FWHM)*. The finesse $\tilde{F}$ of a Fabry-Perot interferometer is defined as the quotient of *FSR/FWHM* and often used as figure of merit. Simple relations for the center wavelength λ_m, the free spectral range *FSR*, the full-width at half-maximum *FWHM* und the finesse $\tilde{F}_R$ (finesse in terms of reflectance) can be deduced using air as resonator medium, under the condition of normal incidence and by neglecting the effect of phase shift at the reflectors φ. In table 1 these functions and additionally the requirements for the filter and the resulting design parameters are listed.

Table 1. Mathematical description, requirements and design of a Fabry-Perot Filter

	$y = f(\sigma)$	$y = f(\lambda)$	**Requirement**	**Design Parameter**
Center Wavelength	$\sigma_m = \frac{m}{2d}$ (4a)	$\lambda_m = \frac{1}{\sigma_m} = \frac{2d}{m}$ (4b)	$\lambda_m = 5...3\mu m$	$\frac{d}{m} = 2.5...1.5\mu m$
Free Spectral Range	$FSR_\sigma = \frac{1}{2d}$ (5a)	$FSR_\lambda = \frac{\lambda_m}{m+1} = \frac{\lambda_{m+1}}{m}$ (5b)	$FSR_\lambda = 2\mu m$	$m = 1$
Full Width Half Maximum	$FWHM_\sigma = \frac{1}{2d\pi}\frac{1}{\tilde{F}_R}$ (6a)	$FWHM_\lambda = \frac{\lambda_m}{m}\frac{1}{\tilde{F}_R}$ (6b)	$FWHM_\lambda = 50...100\ nm$	$\tilde{F}_R = 40...80$
Reflective Finesse	$\tilde{F}_R = \frac{FSR}{FWHM} = \frac{\pi\sqrt{R}}{1-R}$ (7)			$R = 0.924...0.962$
Contrast	$C = \frac{T_{max}}{T_{min}} = \frac{(1+R)^2}{(1-R)^2}$ (8)		$C \geq 400$	$R \geq 0.905$

The tunability of the filter between 5 µm and 3 µm requires an order number *m = 1* and a physical tuning of the resonator cavity from 2500 nm to 1500 nm. Bandwidths of 100…50 nm require a finesse between 40…80 or a reflectance of about 92.4…96.2 %, where a transmission contrast of at least 400 can be obtained.

2.2 Mechanical design

In order to achieve the tuning of the resonator cavity, an electrostatic actuation using a parallel plate design has been chosen. It fits very well the filter set-up and can be easily integrated. Due to these advantages electrostatic actuators are the most common micromachined drives /5, 6/. However, the achieved forces are lower in comparison to piezoelectric drives /7/, which on the other hand need additional materials, that are difficult to integrate in the micromachining.

The design principle of the detector with tunable filter is shown in figure 3. It is based on an approach using relatively thick reflector carriers, one of them being fixed and the other suspended by springs which allow vertical movement. The mechanically stiff reflectors with low curvature guarantee a high finesse and a high aperture. The filter design is compatible to micromachining technology. A set-up of coated and etched wafer is bonded directly or by an intermediate SU-8 layer. This yields in medium fabrication complexity.

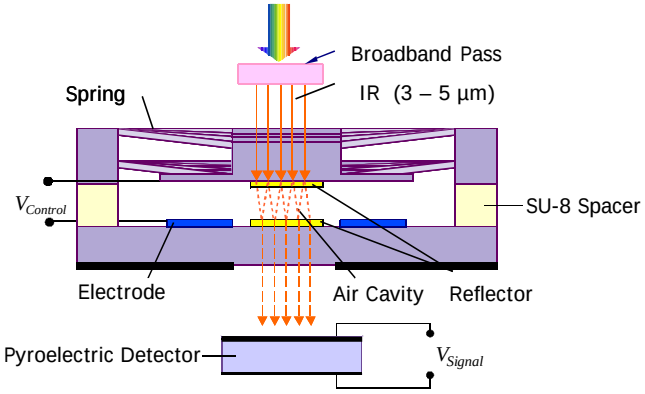

Fig. 3. Design principle of the detector with tunable filter

300 µm thick silicon wafers with a resistivity of 5…10 Ωcm are used as carriers for both the fixed and the movable reflector. The fixed reflector is located in the center surrounded by the driving electrodes. The movable reflector is suspended by diagonally arranged springs located in the corners of the outer frame. Various types of movable reflector and spring configurations, shown in figures 4-6 have been fabricated to determine the optimum solution with respect to maximum tuning range, low gravity influence on center wavelength and filter bandwidth, low deviation of reflector parallelism by mechanical stress and low fabrication complexity. In the first type the movable reflector carrier consists of two wafers with wet etched springs. After direct bonding of the wafer a parallel spring suspension with eight diagonal springs is formed. The parallel spring suspension will provide the necessary vertical movement and the necessary rigidity to minimize any tilting of the movable mirror carrier /8/. In the second type the movable reflector carrier consists of a single wafer. In this case the parallel spring suspension is wet etched from both sides of the wafer. In the third type dry etched springs with stress compensating elements are used instead of the parallel spring suspension, resulting in the most simplified design and technology. The center of gravity of the movable reflector carrier was designed to be in the middle plane between the two bonded wafers and also in the middle of the single wafer in order to prevent tilting by gravity. The outer parts of the movable reflector carrier are used as movable electrodes. The polycrystalline silicon layers of the reflector stacks are connected to the wafer keeping these layers free of electrostatic charges.

The parallel spring design results in a nearly ideal movement in vertical direction. But this is only the case, if the assembling of the planes succeeds tension and warping free. Tensions in lengthwise direction cannot be compensated by the springs. They lead to a deformation of the spring in vertical direction. Alternatively stress compensation elements can be integrated into the springs. The T-form facilitates the reception of tensions in lengthwise direction, as the small T side can be bended crosswise. Advantages of this modification are the simple and proven technology, a large freedom of the design parameters and the high precision of the fabricated springs. The dry etching makes not only possible smaller dimensions of the spring, but also smaller trenches. Thus the spring needs less space even with complicate embodiment and more area can be used for the electrostatic force generation. Combined with a wet etching process for the adjustment of the spring thickness very precise spring mass systems can be produced. According to the actual design parameters, the measured resonance frequencies and the calculated spring stiffness are 7.7 kHz and 13.4 kN/m for the parallel springs and 4.8 kHz and 7.4 kN/m for the stress compensated springs.

Both the wafers with the movable and the fixed reflector carriers respectively are connected either by direct silicon bonding or with a SU-8 interface layer. The direct bonding is carried out after a surface activation in oxygen plasma at room temperature and impact of a marginal mechanical pressure. A sufficient rigidity and long-term stability is achieved by high temperature annealing at 400 °C. This procedure is repeatedly approved, but works well only for a perfect surface quality.

SU-8 is spun-on the wafer like a photoresist. It is offered in different nominal thicknesses, the desired layer thickness can be adjusted by changing the rotation speed of the spinning. For the layer thicknesses requested here a SU-8 with a nominal thickness of 5 µm was chosen. The thickness accuracy of the spinning process was measured to be <100 nm. The bonding was carried out after slow heating at 100 °C under pressure and slow cooling down.

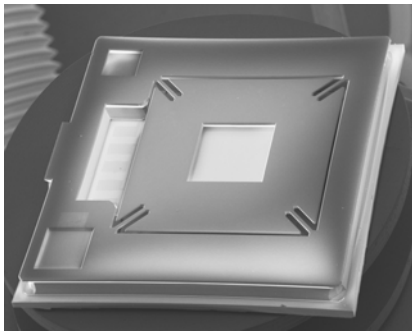

Fig. 4a. SEM image of the movable reflector carrier fabricated by direct bonding of two wafer

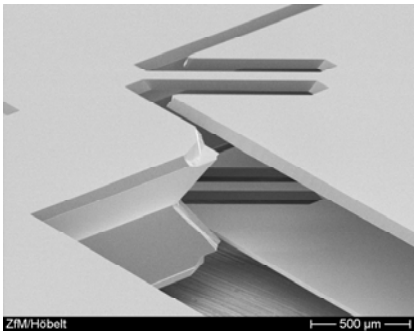

Fig. 4b. SEM image of the parallel spring suspension of the bonded reflector carrier

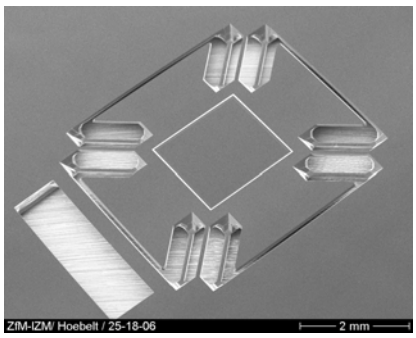

Fig. 5a. SEM image of the single wafer movable reflector carrier fabricated by double-side etching

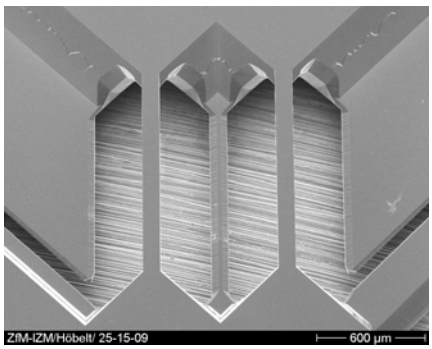

Fig. 5b. SEM image of the parallel spring suspension of the single wafer reflector wafer

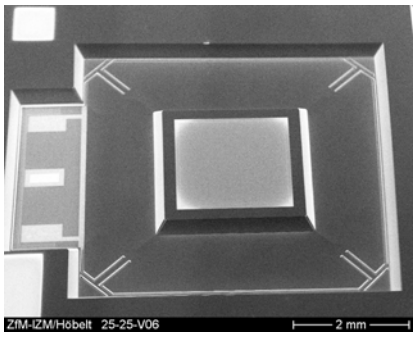

Fig. 6a. SEM image of the single wafer movable reflector carrier fabricated by dry etching

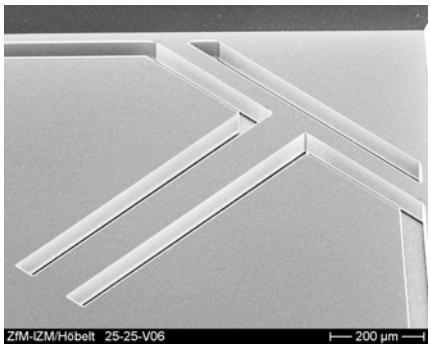

Fig. 6b. SEM image of the dry etched springs with a stress compensating element

3. BRAGG REFLECTOR AND ANTI-REFLECTION COATING DESIGN

Distributed Bragg reflectors are commonly used to generate a broadband reflector /9/. Bragg reflectors are built up by alternating quarter wave optical thickness (QWOT) layers with low and high refractive index. In order to generate a broad high reflective zone from 3…5 µm even with a low stack number, thin films with as high as possible refractive index ratio n_H/n_L have to be applied. Potential thin films are silicon dioxide, silicon nitride and SiO_2 aerogel as low refractive index material and polycrystalline silicon as high refractive index material. The optical constants n and k were measured by an ellipsometer on QWOT layers in the wavelength range of 2…20 µm. The layers are deposited by CVD processes and spin-on technology (aerogel) and compatible with the above described micromachining process. Measured optical constants are plotted versus the wavelength from 2…20 µm within figure 7.

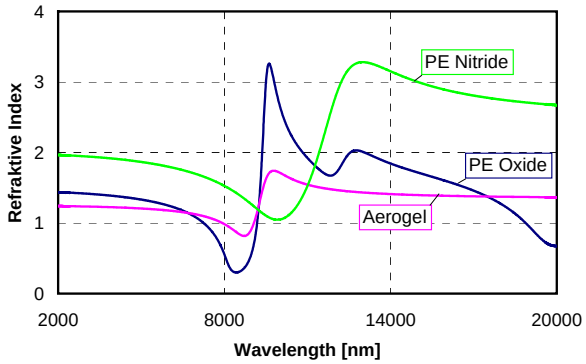

Fig. 7a. Refractive index n of optical thin films

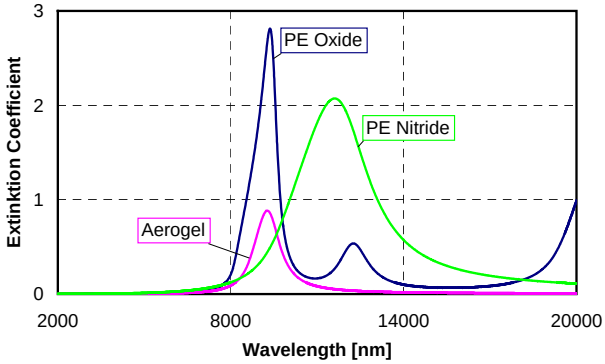

Fig. 7b. Extinction coefficient k of optical thin films

In the 3…5 µm range all investigated thin films are characterized by a very low absorption and a moderate dispersion of the refractive index. The lowest refractive index of 1.22 was shown for aerogel films (highly porous silica), but the spin-on technology is not yet suitable for precise optical coating and structuring. Silicon dioxide with a refractive index of 1.38 at 4 µm is used as low refractive index material and polycrystalline silicon with a refractive index of 3.33 at 4 µm is used as high refractive index material for the reflectors. Silicon nitride was tested as single layer anti-reflection coating (ARC).

Because of the high ratio of refractive indexes n_H/n_L of 2.41 a wide high-reflective zone from 3…5 µm with a high average and maximum reflectance of about 95% and of 96% respectively was obtained already with a $|LH|^2$ layer stack /8/. Increasing the stack number to 3 the average and maximum reflectance increases to 98% and 99% respectively and squares the high reflection zone, but also the roughness of the stack increases /10/. The reason for the stack roughness is the deposition of polycrystalline silicon. Although a reduction of the roughness to 1.3 nm could be obtained by reducing the deposition temperature, etalons with a triple-stack showed a remarkable worse performance. Hence a double-stack $|LH|^2$ was chosen as Bragg reflector and the spectral range of 3…5 µm was divided in two sub-ranges with each 1300 nm from 3.0...4.3 µm und 3.7...5.0 µm. A reference wavelength of 3550 nm was chosen for the short cavity version and 4400 nm respectively for the long cavity version. The physical thickness of the Bragg reflector for both versions is 1760 nm and 2220 nm respectively. In figure 8a and 8b calculated reflectance and phase shift on reflection are plotted for the short and long cavity filter versus wavelength.

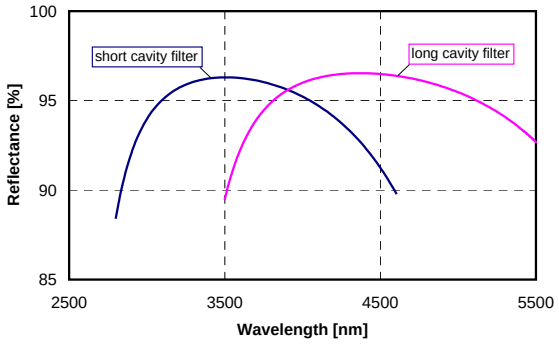

Fig. 8a. Reflectance of distributed Bragg reflectors with optical references at 3550 nm and 4400 nm for short and long cavity filters

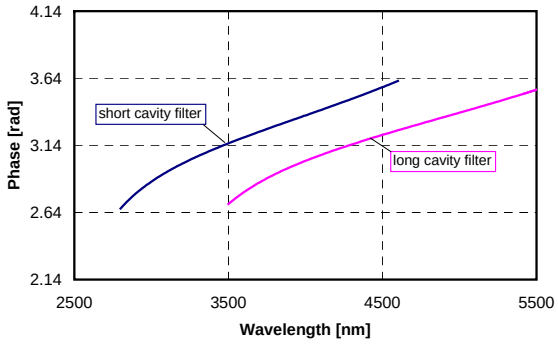

Fig. 8b. Phase shift on reflection of distributed Bragg reflectors with optical references at 3550 nm and 4400 nm for short and long cavity filters

The backsides of the wafer were anti-reflection coated to reduce reflection losses and ripples in the high reflective band caused by multiple reflections in the silicon substrate. A QWOT layer silicon nitride with a refractive index of 1.89 would be a much better silicon ARC than a QWOT layer of silicon dioxide with a refractive index of 1.38 according to equation (9):

$$n_L = \left(n_0 n_S\right)^{1/2} \tag{9}$$

which results in a refractive index n_L of 1.85 for a silicon/air interface at a wavelength of 4 µm. Unfortunately silicon nitride layers exhibit high intrinsic stress, which produces substrate bowing after deposition, and therefore make them unsuitable for anti-reflection coatings of FP filters. Alternatively a double-layer broadband ARC increases the transmittance in a broader wavelength range. The refractive indexes of the QWOT double-layer ARC must follow equations (10) and (11) /9/:

$$n_1 = \left(n_0^2 n_S\right)^{1/3} = 1.51 \tag{10}$$

$$n_2 = \left(n_0 n_S^2\right)^{1/3} = 2.27 \tag{11}$$

This double-layer design was refined to use only silicon dioxide and polycrystalline silicon layers for the ARC too. For the first layer a QWOT silicon dioxide layer with n_1 of 1.38 of was chosen. The second layer was synthesized with very thin films of silicon dioxide and polycrystalline silicon fulfilling the condition $nd << \lambda$ /11/.

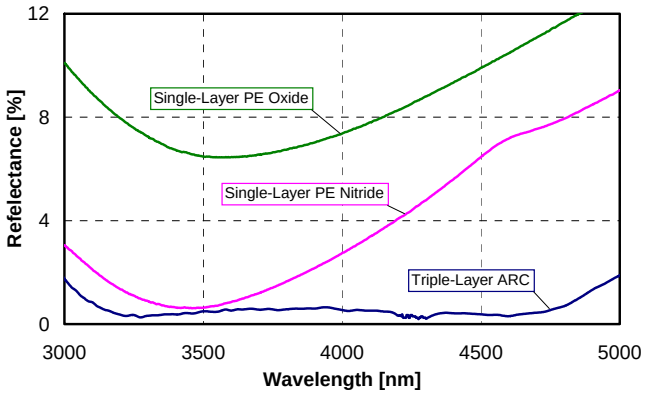

Fig. 9. Reflectance of single and triple-layer layer anti-reflection coating

The overall physical thickness of the refined triple-layer broadband ARC is only about 1000 nm. In figure 9 the single-layer ARC is compared with the broadband triple-layer ARC. Whereas the reflectance of the single-layer ARC has a minimum only at the reference wavelength the reflectance of the refined triple-layer ARC has an average of 0.6% in the hole spectral range of 3…5 µm and a minimum of 0.3%.

The necessary air gap size of the short and long cavity Fabry-Perot filters were designed with a commercial optical thin film software /12/ considering the influence of the additional phase shift φ, which appears by the reflection at the dielectric reflectors.

Although the correlation of center wavelength versus the cavity spacing is determined by a slope of 2 for perfect reflectors without additional phase shift, the actual design shows a slope of 1.3 considering the phase shift (fig. 10).

This increases the necessary cavity tuning to 135% compared to perfect reflectors. It makes clear, that the influence of the phase shift φ can not be neglected for small interference orders. The mismatch of both functions is caused by different absolute phase shifts because of different design wavelengths, already shown in figure 8b.

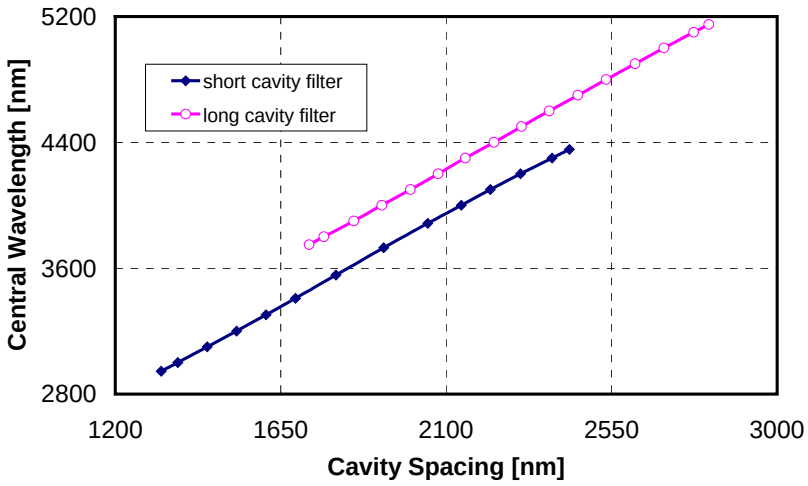

Fig. 10. Simulated dependence of the center wavelength of the peak transmittance from air cavity spacing of short and long cavity filters

4. DETECTOR DESIGN

The tunable filter is arranged on top of a current mode pyroelectric detector with a flat spectral response, shown in figure 11. The transimpedance amplifier (TIA) is connected to a blackened 2x2 mm² pyroelectric chip of lithium tantalate, which is the radiation sensitive element. A second chip, which is connected anti-parallel and shielded from the radiation, compensates signals due to temperature changes of the surroundings and of the package without reducing the responsivity /13/. A low noise, low power CMOS op-amp with a 100 GΩ feedback resistance and a very low parasitic 40 fF feedback capacitance converts the pyroelectric current into a high signal voltage. The op-amp operates with a minimum supply voltage of ±2.2 V and a quiescent current of 70 µA. The low power dissipation in connection with the thermal compensation results in a very short warm-up time of several seconds. To avoid capacitive coupling from the electrostatic driving circuitry of the tunable filter the pyroelectric chips and the input of the TIA are completely shielded. The wiring of the detector is shown in figure 12.

Both the tunable filter and the detector are packaged in a TO-8 housing with a broad bandpass filter. The broad bandpass filter transmits only in the 3.0…4.3 µm range for the short cavity filter and 3.7…5.0 µm range for the long cavity filter and blocks higher interference orders and long wave radiation from UV…12 µm

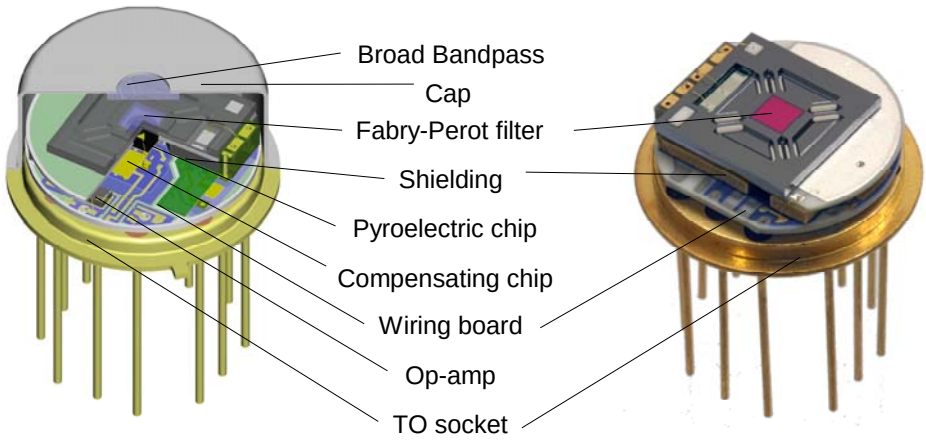

Fig. 11. Schematic drawing (left) and picture of a sample (right) of a tunable pyroelectric detector with integrated filter

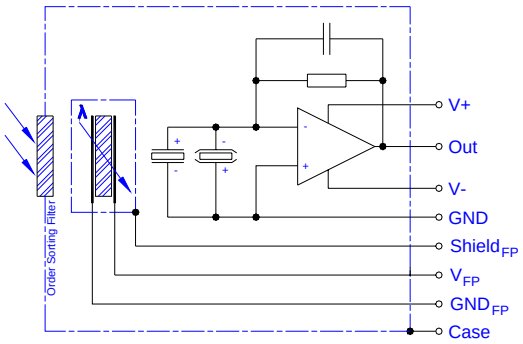

Fig. 12. Wiring of the tunable pyroelectric detector with integrated filter

5. DETECTOR PERFORMANCE

The transmittance of the Fabry-Perot filters was measured using a FT-IR interferometer at a resolution of 8 cm^{-1} before packaging into the detector. The results of the optical measurements of the short and long cavity filters presented in figures 13 and 14 confirm the optical design to achieve a high transmittance and a low bandwidth.

The typical bandwidths *FWHM* of the long cavity and short cavity filters are 100±20 nm and 80±20 nm respectively. The voltage dependence of the filter's *CWL* features the typical square root function of an electrostatic actuator. The decreasing transmittance during tuning is a result of the moveable reflectors tilting, which is induced from spring stiffness and electrode area inhomogeneities. The different design approaches with spring stiffnesses of 13.4 kN/m and 7.4 kN/m result in different maximum driving voltages of 60 V and 27 V respectively to provide a tuning range of about 1300 nm.

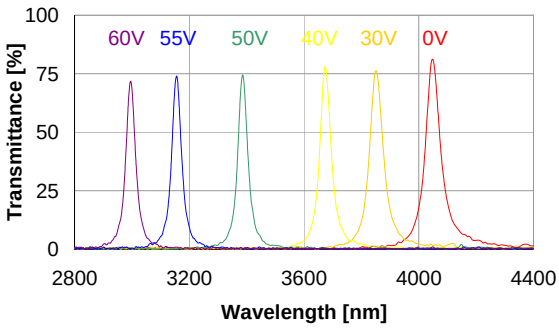

Fig. 13a. Spectral transmittance of a short cavity FP filter with high stiffness parallel springs

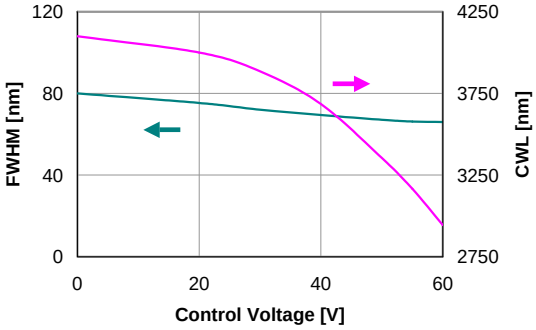

Fig. 13b Bandwidth and center wavelength of a short cavity FP filter with high stiffness parallel springs

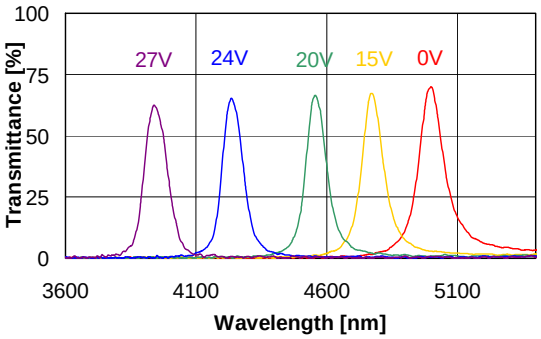

Fig. 14a. Spectral transmittance of a long cavity FP filter with low stiffness compensating springs

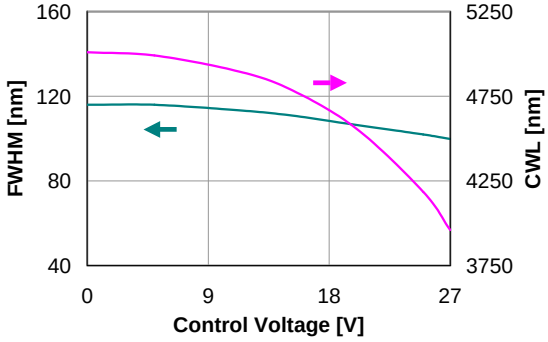

Fig. 14b. Bandwidth and center wavelength of a long cavity FP filter with low stiffness compensating springs

The voltage responsivity and the noise density of the tunable detector are presented in figures 15a and 15b. As a result of the low electrical time constant of 4 ms the normalized responsivity is flat up to a frequency of 40 Hz. The responsivity R_V *(400°C, 10 Hz, 25°C)* of the detector including the tunable filter is about 1250 V/W and 160,000 V/W for the detector without the tunable filter respectively. The specific detectivity of the tunable detector is higher than $4 \cdot 10^6$ cmHz$^{1/2}$/W.

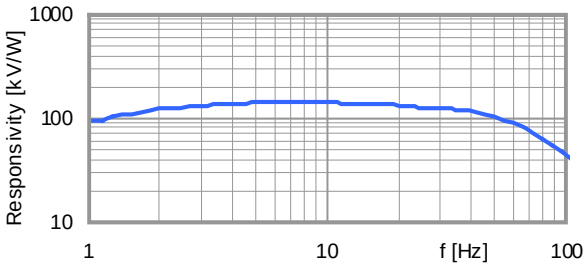

Fig. 15a. Responsivity of the tunable detector

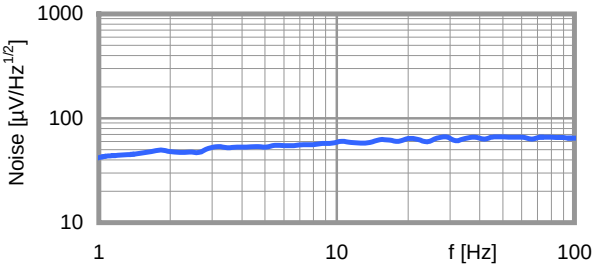

Fig. 15b. Noise density of the tunable detector

Tunable detectors and stand-alone filters were applied in infrared analyzers and spectrometers to quantify single gases like ethanol and carbon dioxide as well as gas mixtures of methane and propane and anesthetic gases of halothane, laughing gas and different fluranes. The tests confirmed the higher performance and flexibility of the tunable detector approach in comparison to detectors equipped with fixed narrow band filters.

6. DISCUSSION

Comparing the measured finesse and the peak transmittance of the FP filters with the theoretical data, the influence of defects (deviations from the ideal filter characteristic) can be evaluated by introducing an effective finesse $\tilde{F}_E$ /14, 15/. The effective finesse $\tilde{F}_E$ can be understood as quadratic interaction of the distinct terms $\tilde{F}_X$:

$$\tilde{F}_E = \left[\frac{1}{\Sigma \tilde{F}_X^2} \right]^{-1/2} \qquad (12)$$

with the reflective finesse $\tilde{F}_R$, the spherical finesse $\tilde{F}_S$, the roughness (Gaussian) finesse $\tilde{F}_G$ and the parallelism finesse $\tilde{F}_P$. The collimation finesse shall not be considered here.

The reflective finesse $\tilde{F}_R$ can be calculated with equation (7) and is 77 for a reflectance *R* of 0.96.

For the terms of the effective finesse $\tilde{F}_X$ caused by the defects δ_X the following relations could be deduced:

spherical finesse $$\tilde{F}_S = \frac{\lambda}{2\delta_S}, \tag{13}$$

roughness (gaussian) finesse $$\tilde{F}_R = \frac{\lambda}{22^{1/2}\delta_G}, \tag{14}$$

parallelism finesse $$\tilde{F}_P = \frac{\lambda}{3^{1/2}\delta_P}, \tag{15}$$

Assuming that a degradation of the effective finesse to 90 % compared to the reflective finesse ($\tilde{F}_R$ of 77) could be accepted, the defect terms $\tilde{F}_X$ should be greater than 275. Therefore considering equations 13-15 at a wavelength of 4 µm the warping δ_S should be less than 7.3 nm, the roughness δ_R smaller than 3.1 nm and the tilting δ_P smaller than 8.4 nm. This is a great challenge in combination with an aperture of 2x2 mm^2. As however the effective finesse $\tilde{F}_E$ is determined by the smallest term $\tilde{F}_X$, the definition of the major defect δ_X is essential for the practical application.

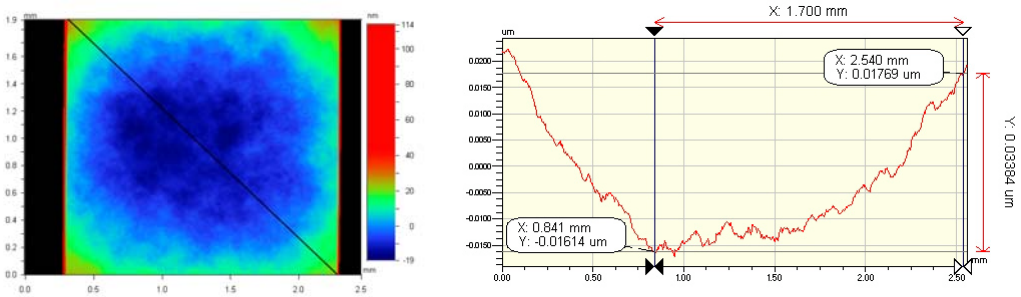

Fig. 16. Flatness measurement results on optical active area (measured by WYKO NT1100)

Although the roughness of the dielectric layer stacks $|LH|^2$ could be reduced to 1.7 nm due to an improved deposition of the polycrystalline silicon, the warping δ_S measures typical 35 nm (shown in figure 16) reducing the defect term $\tilde{F}_S$ to 57. Even without including a tilting δ_P, a dramatic decrease of the effective finesse $\tilde{F}_E$ to 45.6 has to be noticed. This leads to an increase of the bandwidth to 86 nm at 4 µm wavelength and respectively 107 nm at 5 µm wavelength. These calculated bandwidths conform well to the measured typical bandwidths. Therefore, we can conclude that mainly the warping of the reflectors essentially determines finesse and bandwidth. Further effort should be put on reducing this warp by optimization of the layer deposition process, because it is mainly caused by stress in the silicon dioxide layers.

ACKNOWLEDGMENT

This project was supported by the European Regional Development Fund 2000-2006 and by the Ministry for Economy and Labor of Saxony.

REFERENCES

1. J. Staab, *Industrielle Gasanalyse*, Oldenbourg, München und Wien, 1994.
2. Atmospheric transmission calculating program, *USF HITRAN-PC V2.41*, University of South Florida, 1995
3. M. Blomberg,. O. Rusanen, K. Keranen, A. Lehto, „A silicon microsystem-miniaturised infrared spectrometer", Proc. 9th Int. Conf. on Solid-State Sensors, Actuators and Microsystems, 1257-1258 (1997), Chicago, U.S.A., June 16-19, 1997.
4. E. Hecht, *Optik*, Oldenbourg, München und Wien, 2005.
5. J.H. Jerman, D.J. Clift and S.R. Mallinson, "A miniature Fabry-Perot interferometer with corrugated silicon diaphragm support", *Sensors and Actuators A*, 29, 151-158 (1991).
6. D. Rossberg, "Silicon micromachined infrared sensor with tunable wavelength selectivity for application in infrared spectroscopy", *Sensors and actuators A*, 46-47, 413-416, (1995).
7. J. T. Knudtson, D. S. Levy, K. C. Herr, "Electronically tunable, first-order Fabry-Perot-infrared filter" , *Opt. Eng*. 35(8), 2313-2320 (1996).
8. S. Kurth, K. Hiller, N. Neumann, M. Heinze, W. Dötzel, T. Geßner, "A tunable Fabry-Perot-Interferometer for 3–5 µm wavelength with bulk micromachined reflector carrier", *Proc. of SPIE*, 4983, 215-226 (2003).
9. H.A. Macleod, *Thin-Film optical filters*, IoP, Bristol and Philadelphia, 2001.
10. N. Neumann, K. Hiller and S. Kurth, „Micromachined Mid-Infrared Tunable Fabry-Perot Filter", Proc. 13th Int. Conf. on Solid-State Sensors, Actuators and Microsystems, 1010-1013 (2005) Seoul, Korea, June 5-9, (2005).
11. W.H. Stockwell, "Coating design using very thin high- and low-index layers", *Appl. Optics* 24(4), 457-460 (1985).
12. Optical coating design program, *Essential Macleod V8.9*, Thin Film Center Inc., Tucson.
13. N. Neumann, H.-J. Stegbauer, H. Sänze, M. Gürtner, F. Schneider, „Application of fast response dual-colour pyroelectric detectors with integrated op amp in a low power NDIR gas monitor", Proc. 8th Int. Conf. for Infrared Sensors and systems, IRS2, 183-188 (2004), Nuremberg, Germany, 25-27 May, 2004.
14. E. Palik, H.Boukari, R. Gammon, "Experimental study of the effect of surface defects on the finesse and contrast of a Fabry-Perot interferometer", Appl. Optics, 35(1), 38-50, (1996).
15. G. Hernandez, *Fabry-Perot Interferometers*, Cambridge University Press, Cambridge, 1986.

MOEMS-MEMS 2007

Part of SPIE Photonics WEST

Honorable Mention

presented to

Norbert Neumann

InfraTec GmbH

For the outstanding presentation of paper 6466-5 *on*
Tunable infrared detector with integrated micromachined Fabry-Perot filter

Presented at the conference on
MOEMS and Miniaturized Systems VI

Attested by
David Dickensheets
Bishnu Gogoi
Harals Schenk
Conference Chairs

January 2007